## PAPER

Check for updates

# H$_2$O and CO$_2$ surface contamination of the lithium garnet Li$_7$La$_3$Zr$_2$O$_{12}$ solid electrolyte†

Yuheng Li, [iD] [a] Asmee M. Prabhu, [b] Tej S. Choksi [iD] *[b] and Pieremanuele Canepa [iD] *[ac]

Understanding the reactivity of ubiquitous molecules on complex oxides has broad impacts in energy applications and catalysis. Garnet-type Li$_7$La$_3$Zr$_2$O$_{12}$ is a promising solid-state electrolyte for lithium (Li)-ion batteries, and it readily reacts with H$_2$O and CO$_2$ when exposed to ambient air. Such reactions form a contamination layer on Li$_7$La$_3$Zr$_2$O$_{12}$, which is detrimental to the battery operation. The strong interactions of Li$_7$La$_3$Zr$_2$O$_{12}$ with H$_2$O and CO$_2$, however, make Li$_7$La$_3$Zr$_2$O$_{12}$ a promising support to catalyze H$_2$O dissociation and CO$_2$ adsorption. Here, using first-principles calculations, we investigate the adsorption and reactions of H$_2$O and CO$_2$ on a Li$_7$La$_3$Zr$_2$O$_{12}$ surface. We show that H$_2$O reacts through the exchange of protons and Li$^+$ and produces metal hydroxide species. At high H$_2$O coverage, half of the H$_2$O molecules dissociate, while the other half remain intact. CO$_2$ reacts with the Li$_7$La$_3$Zr$_2$O$_{12}$ surface directly to produce carbonate species. We clarify that the individual reactions of H$_2$O and CO$_2$ with Li$_7$La$_3$Zr$_2$O$_{12}$ are more thermodynamically favorable than the co-adsorption of H$_2$O and CO$_2$. Finally, we demonstrate that low temperature and high partial pressure promote the reactions of H$_2$O and CO$_2$ with Li$_7$La$_3$Zr$_2$O$_{12}$. For the energy storage application of Li$_7$La$_3$Zr$_2$O$_{12}$, our study provides processing conditions to minimize surface contamination. From a catalysis point of view, our findings reveal the potential of using complex oxides, such as Li$_7$La$_3$Zr$_2$O$_{12}$, as a support for reactions requiring H$_2$O dissociation and strong CO$_2$ adsorption.

## 1. Introduction

Energy storage and conversion devices relying on complex oxides are central to the decarbonization of our planet.[1–4]

On one hand, lithium(Li)-ion batteries based on oxide chemistries[1,5] offer an appealing strategy to store green energy produced by photo-voltaic panels, wind turbines, hydropower and/or hydroelectric means. Li batteries suffer from safety issues, mostly due to the flammability of liquid electrolytes.[1] Solid-state batteries, replacing the flammable electrolyte with a solid "ceramic" – solid electrolytes – are safer alternatives.[6–9] When suitably doped, the garnet-type quaternary oxide Li$_7$La$_3$-Zr$_2$O$_{12}$ as a solid electrolyte achieves unprecedented Li$^+$ conductivities ($\sim 10^{-6}$–$10^{-3}$ S cm$^{-1}$).[10–24] Importantly, Li$_7$La$_3$Zr$_2$O$_{12}$

is claimed to be stable against high-energy density Li-metal anodes, which is an appealing feature for high-energy density batteries enabling vehicular transportation.[20,22–25]

On the other hand, complex oxides catalyze the decomposition of abundant molecules, such as H$_2$O and CO$_2$.[26–30] Water dissociation during the water-gas shift reaction is a vital elementary step that is promoted by oxide supports, such as Al$_2$O$_3$, CeO$_2$, CuO, La$_2$O$_3$, Mn$_2$O$_4$, TiO$_2$, Y$_2$O$_3$, ZrO$_2$, etc.[31–37] Complex oxides are extensively studied as catalytic supports to adsorb CO$_2$ from dilute gas streams and subsequently transform CO$_2$ into valuable chemicals.[36,38–43]

Here, using Li$_7$La$_3$Zr$_2$O$_{12}$ as an example, in the framework of *ab initio* thermodynamics, we investigate the reactivity of this complex oxide with two ubiquitous molecules: H$_2$O and CO$_2$. Previous work by Sharafi *et al.* using Raman and X-ray photo-emission spectroscopy (XPS) revealed the existence of thick layers ($\sim$5–10 nm) of Li$_2$CO$_3$ on the Li$_7$La$_3$Zr$_2$O$_{12}$ surfaces, upon exposure to air.[21,23] The same authors also detected LiOH on the Li$_7$La$_3$Zr$_2$O$_{12}$ particles. The cartoon of Scheme 1 shows the reaction pathways of CO$_2$ and H$_2$O with Li$_7$La$_3$Zr$_2$O$_{12}$, as proposed in previous bulk-material calculations by Sharafi *et al.*[19] using density functional theory (DFT).

Nevertheless, the complexity of Li$_7$La$_3$Zr$_2$O$_{12}$ (and other garnets) in general suggests that considering the reactions of CO$_2$ and H$_2$O beyond the bulk structure is necessary.[19] Specifically, the structural heterogeneity of active sites on low index

*[a]Department of Materials Science and Engineering, National University of Singapore, 9 Engineering Drive 1, 117 575, Singapore. E-mail: pcanepa@nus.edu.sg*

*[b]School of Chemical and Biomedical Engineering, Nanyang Technological University, Singapore 637 459, Singapore. E-mail: tej.choksi@ntu.edu.sg*

*[c]Department of Chemical and Biomolecular Engineering, National University of Singapore, 4 Engineering Drive 4, 117 585, Singapore*

† Electronic supplementary information (ESI) available: (i) benchmark tests on the effect of vdW corrections, (ii) convergence tests of slab calculations, (iii) structure of the slab unit cell, (iv) tests on single-point energy cutoffs, (v) the description of the metal sites' local environment and H$_2$O dissociation, (vi) calculation results for forced H$_2$O dissociation at high coverage, (vii) geometry of surface carbonates formed at the surfaces and Li$_2$CO$_3$, and (viii) Mulliken charges of sites post-adsorption. See DOI: 10.1039/d1ta10228a
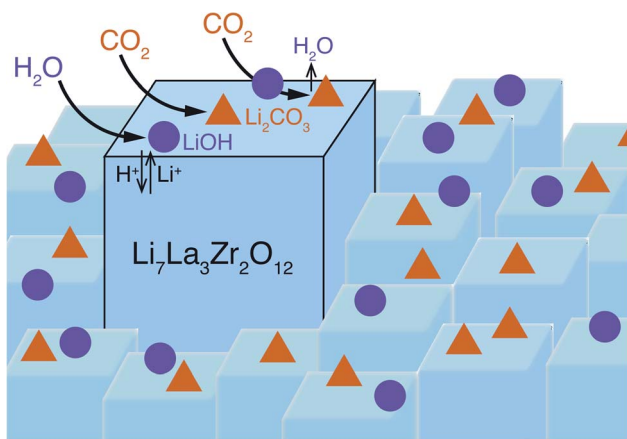
**Scheme 1** Possible reaction pathways for $Li_7La_3Zr_2O_{12}$ particle contamination when exposed to $H_2O$ and $CO_2$.

crystal planes, which contributes to activating closed shell species such as $CO_2$ and $H_2O$, requires detailed exploration of the reactions on surface. Here, we investigate this complex reactivity using DFT calculations of $Li_7La_3Zr_2O_{12}$ slabs interacting with $H_2O$ and $CO_2$. The computed surface phase diagrams reveal that at room temperature and ambient pressures $H_2O$ is adsorbed vigorously on the exposed Li sites at the $Li_7La_3Zr_2O_{12}$ surface, nucleating LiOH and protons. These protons are then exchanged with the highly mobile $Li^+$ ions and may "intercalate" in the $Li_7La_3Zr_2O_{12}$ bulk.[14] Likewise, our simulations demonstrate that $CO_2$ is adsorbed on the $Li_7La_3Zr_2O_{12}$ surface and readily transforms into carbonate species.

If $Li_7La_3Zr_2O_{12}$ is to be used in battery devices, our simulations provide guidelines to curb its degradation by $CO_2$ and $H_2O$. In contrast, spontaneous $H_2O$ dissociation on $Li_7La_3Zr_2O_{12}$ makes it potentially relevant for the water-gas shift reaction,[44,45] while the strong chemisorption of $CO_2$ makes $Li_7La_3Zr_2O_{12}$ a promising dual functional material for $CO_2$ capture and conversion.[46,47] Hence, in the context of catalysis, $Li_7La_3Zr_2O_{12}$ appears to be an excellent catalyst support to investigate the reactions of $CO_2$ activation and water splitting, respectively. These results are important to chart the reactivity of this complex quaternary oxide, which may be extended to other complex oxides.

## 2. Computational methods

The chemical reactions at the surface of $Li_7La_3Zr_2O_{12}$ were probed with Kohn–Sham DFT simulations[48] and approximated by the Perdew–Burke–Ernzerhof (PBE) functional.[49] van der Waals (vdW) interactions were treated with the D3 method with a Becke–Johnson (BJ) damping term.[50–52] The wavefunctions were expanded as plane waves and core electrons by the projector-augmented wave (PAW) method as in VASP.[53–56] The PAW potentials and the recommended cutoff energies were: C 08 Apr 2002 400 eV, H 15 Jun 2001 250 eV, La 06 Sep 2000 219 eV, Li_sv 23 Jan 2001 272 eV, O 08 Apr 2002 400 eV, and Zr_sv 07 Sep 2000 230 eV. Slab optimization was performed in two steps: (i) a preliminary PBE and $\Gamma$-point optimization, and (ii) optimization

with PBE + D3-BJ with a $2 \times 2 \times 1$ $k$-mesh and a cutoff energy of 440 eV. The total energy was converged to $1 \times 10^{-5}$ eV per cell and forces acting on atoms to within 0.01 eV $Å^{-1}$. We concluded with final single-point energy calculations at a higher cut-off of 520 eV and integrated over a $4 \times 4 \times 1$ $k$-point grid.

As in this study we probe the adsorption and reactivity of molecules at the surface of $Li_7La_3Zr_2O_{12}$, it is crucial to treat explicitly the effect of vdW forces. vdW interactions were determined by the D3 + BJ method.[50–52] Using these settings, the lattice constants ($a = 13.085$ Å and $c = 12.579$ Å) of tetragonal ($Ia4_1/acd$) $Li_7La_3Zr_2O_{12}$ were used to rescale the (010) slab models from ref. 24. The (010) Li-terminated off-stoichiometric $Li_7La_3Zr_2O_{12}$ model contains 248 atoms and has a surface energy of $\sim$1.34 J $m^{-2}$. The dispersion corrections (D3-BJ) increase the stability of the bulk structure, resulting in an increased surface energy by $\sim$0.50 J $m^{-2}$ compared to ref. 24. A well-converged vacuum size of 15 Å was used to eliminate spurious slab–slab (and adsorbate–adsorbate) interactions along the direction orthogonal to the surface plane.

A bulk-like region of the slab where all atomic positions are fixed was introduced in the middle of the slab models. A 40% bulk-like region was determined from convergence tests on slab total energies (see Fig. S1 in the ESI†), at which the total energy is converged to $\sim$7 meV with relatively modest computational costs. Note that this procedure is commonly applied in surface science and catalysis to reduce significantly the computing time of structure optimization of large slab models.[57] Benchmark tests on $Li_7La_3Zr_2O_{12}$ bulk lattice constants and surface energies were performed to compare the effects of DFT functionals, *i.e.*, PBE, PBE + D3 without damping, and PBE + D3 with BJ damping (see Table S1 of the ESI†).

The coordination numbers and Mulliken charges were derived from the crystal orbital Hamilton populations (COHP) available in the Lobster code.[58] For the COHP calculations, the energy range is set to −15 to 10 eV, and the same basis functions as those in the PAW potentials are used for projections.

The adsorption energy ($\Delta E_{ads}$) was calculated using eqn (1):[59]

$$\Delta E_{ads} = \frac{1}{2n} \left[ E(slab|2nH_2O^{ads}) - E(slab) - 2nE(H_2O^g) \right], \quad (1)$$

where $n = 1$ is the number of adsorbed molecules on each side of the slab model. In eqn (1), we approximated the Gibbs energy of each term by the DFT total energy (*i.e.*, $G \approx E$), thus neglecting the zero point energy, $pV$ and entropy contributions. $E(slab|2nH_2O^{ads})$ is the total energy for the slab adsorbed with $nH_2O$ (on each surface side), $E(slab)$ is the total energy for the clean-surface slab, and $E(H_2O^g)$ is the total energy for $H_2O$ in the gas phase. From eqn (1), a more negative $\Delta E_{ads}$ value indicates a more favorable interaction of the adsorbate with the surface.

The energy changes computed as a function of $H_2O$ (and $CO_2$) coverage are calculated in terms of the Landau grand-potential energy, $\Omega$ of eqn (2).

$$\Omega(x/5 \text{ ML}) = \frac{1}{2A} \left[ G(slab|2xH_2O^{ads}) - (12 - 2x)\mu^{T,P}(H_2O^g) \right], \quad (2)$$

$$\approx \frac{1}{2A}\left[E\left(\text{slab}|2x\text{H}_2\text{O}^{\text{ads}}\right) - 2xTS_{\text{vib}}^T\left(\text{H}_2\text{O}^{\text{ads}}\right)\right.$$
$$\left. - (12 - 2x)\mu^{T,P}\left(\text{H}_2\text{O}^{\text{g}}\right)\right], \qquad (3)$$

where $x$ is the number of sites adsorbed on each surface, $A$ is the surface area, and $T$ and $P$ are the temperature and partial pressure of $\text{H}_2\text{O}$, respectively. $G(\text{slab}|2x\text{H}_2\text{O}^{\text{ads}})$ is the Gibbs free energy of the adsorbed slab and approximated as in eqn (3), by $E(\text{slab}|2x\text{H}_2\text{O}^{\text{ads}})$, the DFT total energy of the slab adsorbing $x\text{H}_2\text{O}$ molecules on each surface. $S_{\text{vib}}^T(\text{H}_2\text{O}^{\text{ads}})$ is the vibrational entropy of the adsorbed $\text{H}_2\text{O}$ (in either a dissociated or an intact form), which is calculated by fixing all atoms except the adsorbate. $\mu^{T,P}(\text{H}_2\text{O}^{\text{g}})$ is the chemical potential of $\text{H}_2\text{O}$ gas approximated by its DFT total energy in vacuum, corrected by the zero-point energy, and scaled to given $T$ and $P$ conditions using the Shomate equation.[60] Then, the change of grand-potential energy $\Delta\Omega$ ($x/5$ ML) at different water coverage is computed using eqn (4) with respect to the clean surface (0/5 ML).

$$\Delta\Omega(x/5\text{ ML}) = \Omega(x/5\text{ ML}) - \Omega(0/5\text{ ML}). \qquad (4)$$

## 3. Results

### 3.1. $\text{Li}_7\text{La}_3\text{Zr}_2\text{O}_{12}$ (010) surface and selection of adsorption sites

Our analysis begins by selecting the energetically most favorable surface cut of $\text{Li}_7\text{La}_3\text{Zr}_2\text{O}_{12}$ from ref. 24. The off-stoichiometry Li-terminated (010) surface (and identical to the (100) and the (001) surfaces) displays the lowest surface energy ($\sim$ $0.87 \pm 0.02$ J m$^{-2}$) and remains stable even at high temperatures ($\sim$1000 K), targeted by typical thermal treatments of these oxides. The (010) surface corresponds to the dominant surface in the computed Wulff shapes of $\text{Li}_7\text{La}_3\text{Zr}_2\text{O}_{12}$, and it is representative of the real $\text{Li}_7\text{La}_3\text{Zr}_2\text{O}_{12}$ particles, either in sintered powders or sheet composites. Here, off-stoichiometric surfaces refer to surfaces where the stoichiometry deviates in composition from the bulk. As described in the Computational methods (Section 2), the (010) surface from ref. 24 was rescaled and recalculated in this study with the incorporation of vdW interactions.

When studying the adsorption of molecules on surfaces, a non-negligible challenge is selecting chemically sound adsorption configurations from the sheer number of imaginable adsorption conformations. This is especially true in complex oxides, such as $\text{Li}_7\text{La}_3\text{Zr}_2\text{O}_{12}$, which contains three chemically distinct cations with varying local coordination environments of the oxygen atoms. We used pymatgen to ease the identification of unique adsorption sites and subsequently construct the initial structure of adsorbates bound to these sites.[61] To prevent the well-known convergence problems of slab calculations in the presence of fictitious electrical dipoles from polar adsorbates ($\text{H}_2\text{O}$ here), we adsorbed molecules on both surface sides.[62]

In order to clarify the mechanisms of $\text{H}_2\text{O}$ and $\text{CO}_2$ reactions with $\text{Li}_7\text{La}_3\text{Zr}_2\text{O}_{12}$, it is first necessary to create appropriate adsorption models by understanding the characteristics of

different active sites on this structurally heterogeneous surface. These characteristics include the proximity of active sites to the $\text{Li}_7\text{La}_3\text{Zr}_2\text{O}_{12}$ surface, their local environment, their Mulliken charges, and their coordination numbers.

Fig. 1(a) and (b) show the side and top views of the off-stoichiometric Li-terminated (010) surface of $\text{Li}_7\text{La}_3\text{Zr}_2\text{O}_{12}$. By defining a range of search, along the non-periodic direction of the slab of $\sim$0.9 Å from the most exposed atom at the surface, we identified 10 on-top surface adsorption sites. These sites show different proximity to the surface; we denote each site according to its element followed by all species bonded to it. Thus, in Fig. 1 seven unique sites out of the 10 were identified: two types of Li sites Li[2O] and Li[3O]; two types of La sites La[5O] and La[6O]; three types of O sites O[LiLaZr], O[Li2La], and O[3Li2La], respectively.

Nominally, positively charged ions, such as Li$^+$ and La$^{3+}$, at the $\text{Li}_7\text{La}_3\text{Zr}_2\text{O}_{12}$ surface will attract negatively polarized parts of the adsorbing molecules and *vice versa*.

Fig. 1(c–e) show the computed Mulliken charges and coordination numbers for all seven types of adsorption sites. Mulliken analysis is an intuitive (but not unique) way of repartitioning the electron charge density on each atom (and orbital) by projecting it onto individual orthonormalized atomic orbitals.[63] The surface sites of each species show similar Mulliken charges, albeit distinct coordination numbers. As expected, Li and La metal sites show positive Mulliken charges. From an adsorption point of view, these sites will behave as Lewis acids in favor of accepting electrons from the oxygen lone pair of $\text{H}_2\text{O}$. Indeed, the reactivity of these cations follows the scale of absolute hardness, $\eta$: Li$^+$ ($\sim$35.1 eV) > La$^{3+}$ ($\sim$15.4 eV) $\gg$ Zr$^{3+}$ ($\sim$5.68 eV),[64,65] with Li$^+$, the most electrophilic cation of the three. Since Zr$^{3+}$ is the least reactive metal of the three, we will not consider its reactivity in the remainder of this study. Oxygen sites reveal their basic character, potentially driving the $\text{CO}_2$ adsorption *via* the C atom. We use this knowledge to guide our understanding of the adsorption and dissociation of $\text{H}_2\text{O}$ and $\text{CO}_2$ on $\text{Li}_7\text{La}_3\text{Zr}_2\text{O}_{12}$.

### 3.2. $\text{H}_2\text{O}$ adsorption and hydroxide formation on $\text{Li}_7\text{La}_3\text{Zr}_2\text{O}_{12}$

Here, we provide the mechanistic insights into $\text{H}_2\text{O}$ adsorption and reactions on the $\text{Li}_7\text{La}_3\text{Zr}_2\text{O}_{12}$ (010) surface to form hydroxide species.

Initially, we investigated the adsorption of a single $\text{H}_2\text{O}$ molecule on the Li-terminated $\text{Li}_7\text{La}_3\text{Zr}_2\text{O}_{12}$ (010) surface. This low coverage analysis enables us to probe the surface characteristics of the surface. For every Li or La site, one $\text{H}_2\text{O}$ was adsorbed on each side of the slab model, which eliminates any potential electrical dipoles caused by polar $\text{H}_2\text{O}$.[62] The adsorption energies ($\Delta E_{\text{ads}}$s) of eqn (1) were computed for all five Li and La sites of Fig. 1.[59]

Notably, the calculated $\Delta E_{\text{ads}}$ indicates a higher tendency of a $\text{H}_2\text{O}$ molecule to adsorb on Li$^+$ sites ($\Delta E_{\text{ads}} = -1.21$ eV) compared to La$^{3+}$ sites ($-0.85$ eV), clearly following the scale of cation absolute hardness reported by Parr and Pearson, with Li$^+$ ($\sim$35.1 eV) > La$^{3+}$ ($\sim$15.4 eV).

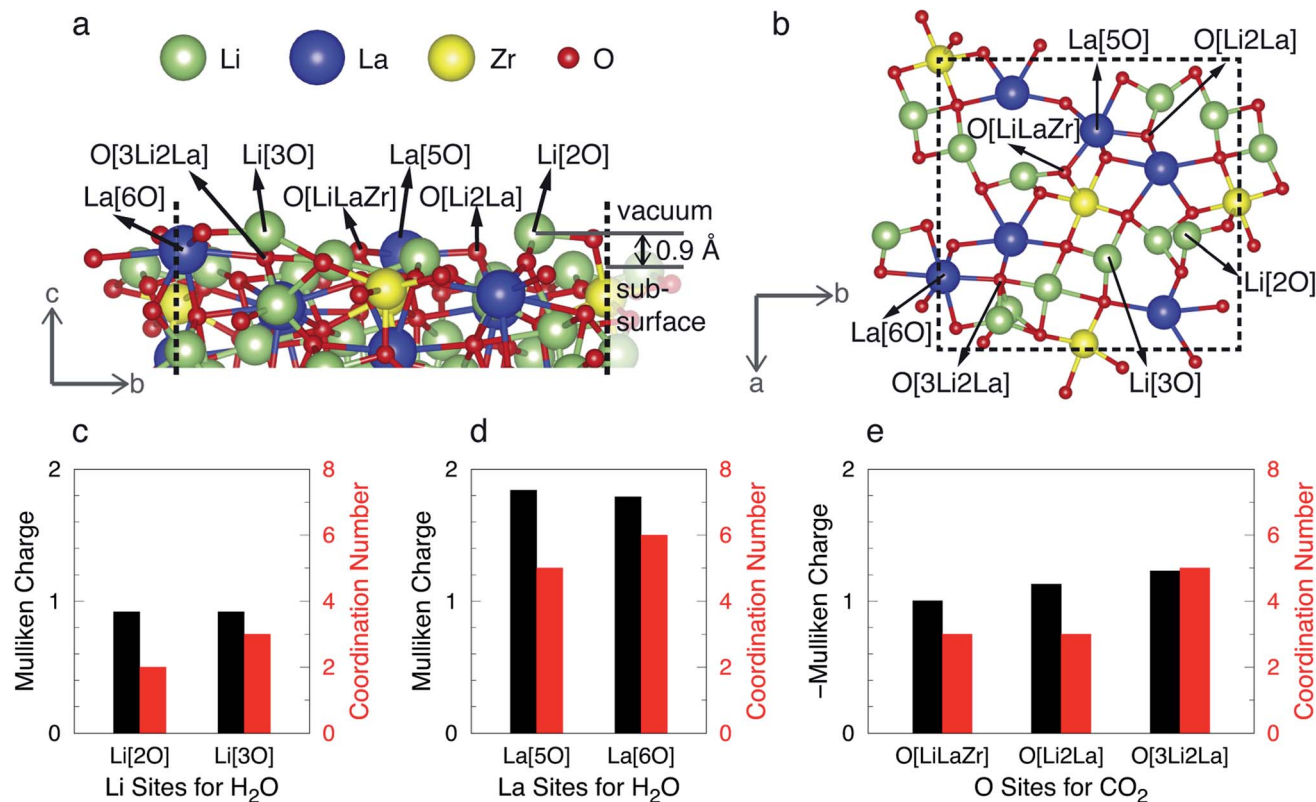Fig. 1 Properties of the adsorption sites on a $Li_7La_3Zr_2O_{12}$ surface. (a) Side view and (b) top view of the off-stoichiometry Li-terminated (010) surface of $Li_7La_3Zr_2O_{12}$. The boundary of the slab unit cell is marked with dashed lines. Li, La, Zr, and O species are shown in green, blue, yellow, and red, respectively. The surface adsorption sites are identified within an ~0.9 Å vertical range (panel (a)). The double headed arrow marks the surface range, outside of which are the vacuum and subsurface. Sites are denoted by the element followed by ions immediately bonded to the site. The 7 unique sites are: 2 types of Li (Li[3O] and Li[2O]), 2 types of La (La[6O] and La[5O]), and 3 types of O (O[3Li2La], O[Li2La], and O[LiLaZr]), respectively. For a clearer view of the sites local environments, we concealed atoms far away from the surface. Mulliken charges (black bars) and coordination numbers (red bars) for Li sites in (c), La sites in (d), and O sites in (e). Li and La sites show positive Mulliken charges, indicating their electro-positive character, and *vice versa* for O sites.

Fig. 2 shows the diagram of the computed adsorption energies and a magnification of the adsorption sites for the two most favorable adsorption cases, which always occur on exposed Li sites.

For the most favorable Li[3O] site (dark green line), $H_2O$ dissociates accompanied by a significant $\Delta E_{ads}$ (~−1.21 eV), and reacts with the Li site to form LiOH (see the lower inset of Fig. 2). Upon $H_2O$ dissociation, a $OH^-$ group is formed between the proton released and an adjacent oxygen atom of the surface; the $OH^-$ group forms a hydrogen bond with the O of the LiOH formed on the Li[3O] site. In the 2nd most favorable Li[2O] site (see the upper inset of Fig. 2), the adsorbed $H_2O$ remains intact, yielding still a non-negligible $\Delta E_{ads}$ of ~−1.14 eV, but comparatively less favorable than the Li[3O] site by ~70 meV. Notably, we attempted the dissociation of $H_2O$ on the Li[2O] site with a calculated $\Delta E_{ads}$ of ~−1.18 eV, indicating that the dissociation is thermodynamically favorable by ~−40 meV with respect to non-dissociative adsorption at these sites.

It is important to unearth the causes behind the significant magnitudes of $\Delta E_{ads}$s and dissociation behaviors of $H_2O$ on different metal sites. We observed that if the coordinates of the surface sub-layers and the inner region of the surface (making

~80% of the slab) are held frozen to those of the bulk slab, the adsorbed $H_2O$ will not dissociate on any site, regardless of its chemical activities. Clearly, with such a constraint in place, the adsorption energy does not benefit from the reorganization of
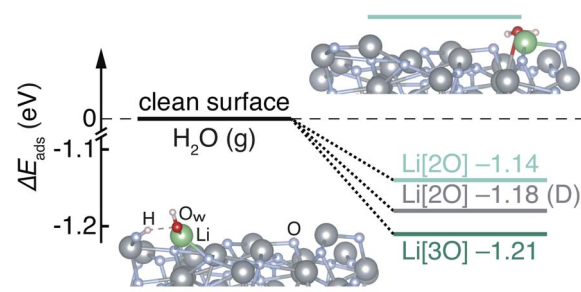


Fig. 2 Adsorption energy for $H_2O$ on the two most favorable sites Li [2O] (light green) and Li[3O] (dark green) on the Li-terminated $Li_7$-$La_3Zr_2O_{12}$ (010) surface. The $H_2O$ molecule on Li[2O] remains intact after adsorption (upper inset), while $H_2O$ on Li[3O] dissociates to form LiOH (lower inset). The grey Li[2O] level marked with a "(D)" shows adsorption energy for a model where we forced $H_2O$ dissociation on the Li[2O] site. Atomic species not directly involved in the adsorption are greyed out.

the surface atoms, which promotes the dissociative adsorption of $H_2O$. Thus, the adsorption energy follows the trend of the site exposure to the surface, with the top (bottom) site showing the most negative adsorption energy. In contrast, by constraining only 40% of the slab model, as in the rest of this study, the adsorbed $H_2O$ on specific sites readily dissociates during the geometry optimization. Note that such preference for dissociation caused by the rearrangement of atoms in the surface sublayers is rarely seen in metals.

Unsurprisingly, $H_2O$ dissociation lowers the adsorption energy. With a stabilizing contribution arising from $H_2O$ dissociation, the adsorption energy no longer follows the trend of sites proximity to the surface. From top to sub-layer sites in the surface, the adsorption energies are: $-1.14$ eV (Li[2O]), $-1.21$ eV (Li[3O]), $-0.85$ eV (La[5O]), $-0.80$ eV (La[6O]), and $-0.65$ eV (Li[3O]). Furthermore, our results clearly indicate that the dissociation behavior depends on the local environment of the adsorption site. If a specific adsorption configuration displays oxygen atoms in the vicinity of the adsorption site, protons from adsorbed $H_2O$ readily dissociate to bond with the surface oxygen species. The dissociative adsorption of $H_2O$ is well understood in previous studies of metal oxides including rutile-$TiO_2$, anatase-$TiO_2$, and rutile-$RuO_2$.[66–68] In general, we find that adsorbed $H_2O$ tends to dissociate when there are oxygen atoms within $\sim 1.9$ Å of the cation site (Table S2†), unless there are metal ions that can better stabilize $H_2O$ adsorption *via* bonding with O in $H_2O$ (see the inset for Li[2O] in Fig. 2). Therefore, the values of $\Delta E_{ads}$ in $Li_7La_3Zr_2O_{12}$ are clearly affected by (i) the site proximity to the surface and (ii) $H_2O$ dissociation driven by the local environment.

We are also interested in the bonding character of $H_2O$ adsorption (or dissociation) on the $Li_7La_3Zr_2O_{12}$ surface since $H_2O$, a closed shell species, has significantly favorable $\Delta E_{ads}$. First, we determined the dispersion contribution to the adsorption energy by comparing our predictions with (PBE-D3) and without van der Waals contributions, and hence just with GGA PBE.[49] The results show that there is a consistent dispersion contribution of only $\sim 15$–$20\%$ to the total DFT energies. This means that dispersion interactions are not a major source of bonding and indicates a more dominant nature of chemisorption-driven reactions instead of physisorption.

Next, we compared the changes of the Mulliken charges of all Li and La sites and O of $H_2O$ before and after $H_2O$ adsorption (Fig. S3(a and b) in the ESI†). Unlike on reducible oxides (with open-shell d or f transition metals),[69,70] there is no charge transfer between $H_2O$ and the surface sites, which indicates the electrostatic nature of the interaction. These insights agree with previous findings that intrinsic surface electrostatics in an insulating 'ionic' system play a critical role in stabilizing the dangling lone pair of $H_2O$.[71]

We now investigate the adsorption of multiple $H_2O$ molecules to simulate reactions at high water coverage on the $Li_7La_3Zr_2O_{12}$ surface. All five Li and La sites were first ordered according to their individual $H_2O$ adsorption energy, from more negative to more positive. In particular, the order of adsorption energies is Li[3O] ($-1.21$ eV) $<$ Li[2O] ($-1.14$ eV) $\ll$ La[5O] ($-0.85$ eV) $<$ La[6O] ($-0.80$ eV) $<$ Li[3O] ($-0.65$ eV). Following

this order of stability, we adsorbed $H_2O$ on available metal sites achieving a complete $H_2O$ monolayer (ML). For each additional molecule, the structure was relaxed before the next $H_2O$ was adsorbed. After all five sites were adsorbed, we identified an additional Li site, which emerged from the surface re-organization upon increasing water coverage. Eventually, six $H_2O$ molecules were adsorbed on each side of the slab (12 in total).

Table 1 reports the $\Delta E_{ads}$ for $H_2O$ on the (010) $Li_7La_3Zr_2O_{12}$ surface as the exposed metal sites are progressively saturated. We denote the $H_2O$ coverage as the fraction of one monolayer ($x/5$ ML). $\Delta E_{ads}$ for the same adsorption but with all $H_2O$ forced to dissociate is reported in Table S3.†

Table 1 shows that the addition of subsequent $H_2O$ molecules to the $Li_7La_3Zr_2O_{12}$ (010) surface from 1/5 ML to 6/5 ML gradually increases $\Delta E_{ads}$ to more positive values. This progressive increase is mainly caused by the more positive adsorption energy of each site, from $-1.21$ to $-0.65$ eV, dependent on their proximity to the surface and whether $H_2O$ spontaneously dissociates. This increase is also likely due to additional $H_2O$–$H_2O$ interactions as a result of crowding the $Li_7La_3Zr_2O_{12}$ surface, and the progressively neutralized and less reactive surface. Simultaneously, specific adsorption arrangements favor hydrogen bonding with the surface.

Fig. 3(a) shows the energy diagram for all adsorption steps towards high $H_2O$ coverage beyond one monolayer. $\Delta \Omega$ was calculated using eqn (2)–(4) for increasing $H_2O$ coverage at a partial pressure of 1 bar and at 300 K. A negative $\Delta \Omega$ means that $H_2O$ adsorbs favorably on the $Li_7La_3Zr_2O_{12}$ surface. As more $H_2O$ molecules adsorb, $\Delta \Omega$ continuously becomes more negative, indicating that increasing coverage is favorable up to 6/5 ML. This trend also suggests that $H_2O$ can probably adsorb beyond 6/5 ML. We also found a decreasing trend for the absolute difference of $\Delta \Omega$ between consecutive $H_2O$ adsorptions. For example, the absolute difference between $\Delta \Omega$ of 6/5 ML and 5/5 ML is 8.7 meV Å$^{-2}$, less than 10.1 meV Å$^{-2}$ between 1/5 ML and 0/5 ML. This decreasing difference is primarily attributed to the adsorption energy trends of individual sites, as less favored adsorption sites become occupied at higher coverages.

As we only consider adsorption sites within $\sim 0.9$ Å from the surface top (bottom), more adsorption sites may be available. Electrostatic repulsion between adsorbates should have only

**Table 1** $H_2O$ adsorption energy (in eV per molecule) at an increasing number of molecules (ML). The site is the adsorption site. $\delta \Delta E_{ads}$ indicates the change of $\Delta E_{ads}$ upon the addition of a $H_2O$ molecule. The number of dissociated $H_2O$ molecules ($H_2O$) is also indicated. MOH (M = Li/La) indicates whether the addition of a new $H_2O$ molecule promotes metal hydroxide formation

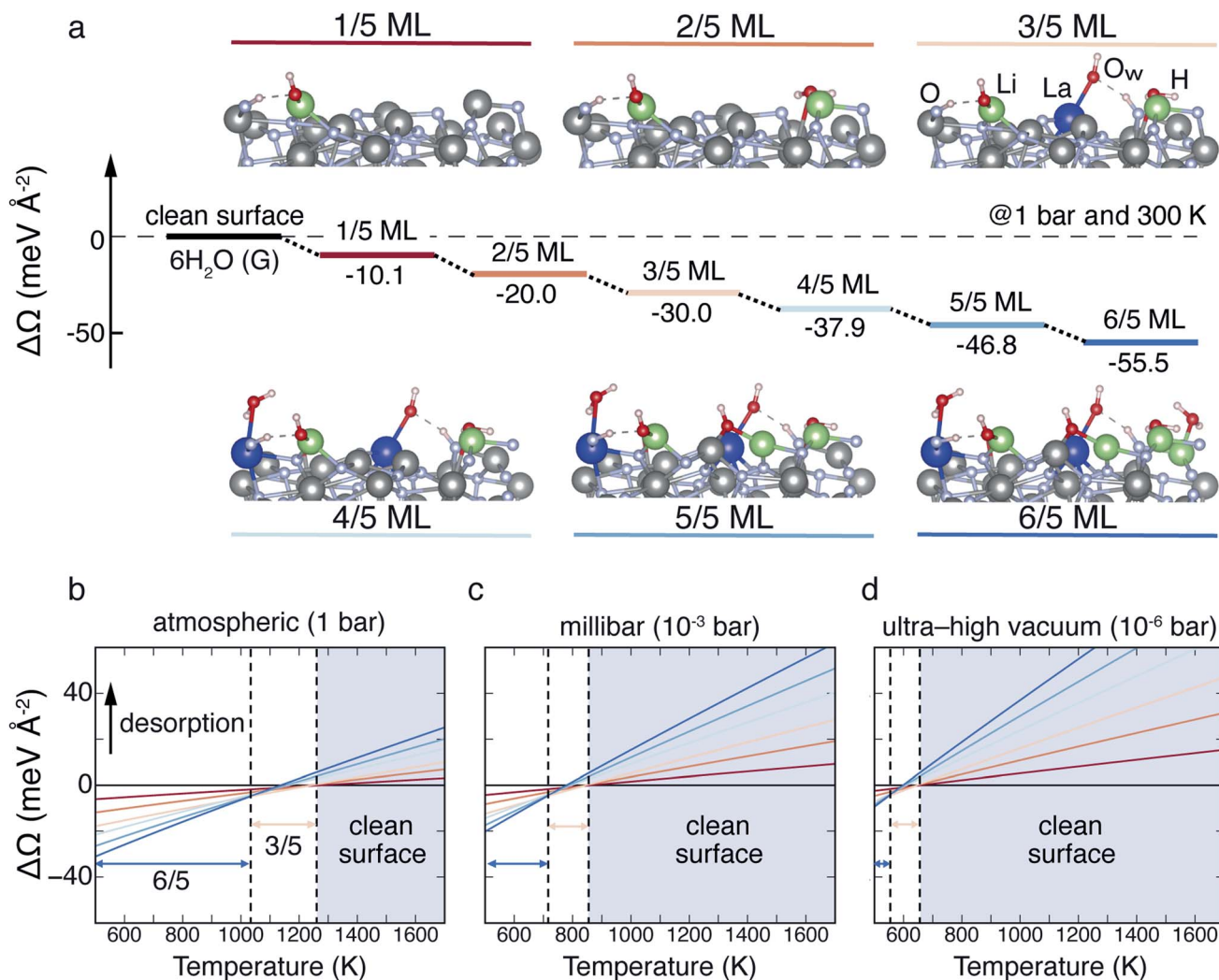| ML | Site | $\Delta E_{ads}$ | $\delta \Delta E_{ads}$ | $H_2O$ | MOH |
|---|---|---|---|---|---|
| 1/5 | Li[3O] | $-1.21$ | — | 1 | Yes |
| 2/5 | Li[2O] | $-1.19$ | $+0.02$ | 1 | No |
| 3/5 | La[5O] | $-1.19$ | $0.00$ | 2 | Yes |
| 4/5 | La[6O] | $-1.10$ | $+0.09$ | 2 | No |
| 5/5 | Li[3O] | $-1.09$ | $+0.01$ | 3 | Yes |
| 6/5 | Li[3O] | $-1.07$ | $+0.02$ | 3 | No |

**Fig. 3** Change of grand-potential energy $\Delta\Omega$ relative to the clean $Li_7La_3Zr_2O_{12}$ surface and gas-phase $H_2O$ at variable temperatures and pressures of technological relevance. In panel (a), the $H_2O$ coverage is denoted by the fraction of a monolayer (ML) of $H_2O$ on the surface. Full coverage is achieved at 6/5 ML when all the five original sites plus an additional site are adsorbed. Increasing coverage is marked by divergent colors from red to blue. $\Delta\Omega$ as a function of temperature for different $H_2O$ coverages and partial pressures of 1 (b, atmospheric regime), $1 \times 10^{-3}$ (c, mbar regime), and $1 \times 10^{-6}$ bar (d, ultra-high vacuum regime). Double arrows show the most favorable coverage within temperature ranges. Atomic species not directly involved in the adsorption are greyed out.

secondary effects on the increasingly more positive values of $\Delta E_{ads}$. Furthermore, a progressive addition of $H_2O$ molecules contributes to gradually neutralizing the highly reactive $Li^+$ sites. Indeed, at a very high water coverage, beyond 6/5 ML, newly adsorbed $H_2O$ molecules may not dissociate, even if dissociation is favored in a single $H_2O$ adsorption on the same site.

For coverage up to 6/5 ML, half of the adsorbed $H_2O$ molecules dissociate and react with the surface to form LiOH (see Table 1). The same happens when all adsorbed $H_2O$ molecules are forced to dissociate before relaxation (see Table S3†). This "half-dissociation" trend was also observed for simple metal oxides like $RuO_2$,[72,73] but a different water dissociation fraction of 75% was observed for the (101) surface in anatase-$TiO_2$.[74] Note that the $H_2O$ dissociation is spontaneous during geometry optimization, and thus it is not necessary to calculate its kinetic

barriers explicitly (expected to be barrier-free). In terms of hydrogen bonding for adsorbates, the dissociated proton always forms hydrogen bonds with the oxygen atom in the original $H_2O$ molecule. All $H_2O$ adsorbates that remain intact form hydrogen bonds with adjacent surface O atoms.

Our analysis of the $H_2O$ reactivity with the $Li_7La_3Zr_2O_{12}$ surface extends to conditions of technological relevance of this material. This analysis is relevant for the optimization of synthesis and heat treatment conditions in $Li_7La_3Zr_2O_{12}$ and common oxides. Fig. 3(b–d) show $\Delta\Omega$ as a function of temperature at atmospheric (1 bar), millibar ($10^{-3}$ bar), and ultra-high vacuum ($10^{-6}$ bar) partial pressures, respectively. The temperature range explored in Fig. 3(b–d) spans those of typical synthesis and sintering temperature ($\sim$1000 °C) of $Li_7La_3Zr_2O_{12}$.[16]

Under atmospheric conditions (Fig. 3(b)), $\Delta\Omega$ at different coverage is plotted in the same color scheme as in Fig. 3(a). A positive $\Delta\Omega$ indicates that adsorbed $H_2O$ is favourable for desorption. We mark the most favorable coverage in different temperature ranges using double headed arrows. In general, as the temperature increases, the $H_2O$ coverage of the surfaces decreases until the surface of $Li_7La_3Zr_2O_{12}$ is water free. This situation is achieved for temperatures above $\sim$1260 K (Fig. 3(b)). At lower temperatures (up to $\sim$1030 K), the most favorable coverage is 6/5 ML $Li_7La_3Zr_2O_{12}$, whereas the 3/5 ML coverage is the most favorable condition in the temperature range 1030–1260 K. Considering even higher coverage, one would expect steeper lines than for 6/5, resulting in a water-rich surface of $Li_7La_3Zr_2O_{12}$. However, such conditions cannot change the scenario for higher temperature ranges ($\geq$1260 K), exhibiting a water-free $Li_7La_3Zr_2O_{12}$ surface.

Under millibar (Fig. 3(c)) and ultra-high vacuum (Fig. 3(d)) $H_2O$ partial pressures, one can find the same general trends for coverage *vs.* temperature as under atmospheric pressure (Fig. 3(a)). However, the temperature range for a water-free clean surface of $Li_7La_3Zr_2O_{12}$ increases as the $H_2O$ partial pressure decreases. For example, in situations of ultra-high vacuum (Fig. 3(d)), we predict an onset temperature of $\sim$650 K, at which the $Li_7La_3Zr_2O_{12}$ surface will be water-free. These findings indicate that low partial pressures are beneficial to minimize surface contamination by $H_2O$ and LiOH.

### 3.3. $CO_2$ adsorption and carbonate formation on $Li_7La_3Zr_2O_{12}$

We now focus on $CO_2$ adsorption on $Li_7La_3Zr_2O_{12}$ and its subsequent transformation into carbonate $CO_3^{2-}$ species. We probed $CO_2$ adsorption on five oxygen sites of the Li-terminated $Li_7La_3Zr_2O_{12}$ surface, as shown in Fig. 1. The adsorption is achieved by placing the carbon atom of $CO_2$ close ($\sim$1.17 Å) to the O site, to induce the formation of a C–O bond. The most favorable site is O[LiLaZr], and its $\Delta E_{ads}$ is strikingly high $\sim$−2.21 eV – a clear indication of $CO_2$ chemisorption. The other sites show comparable ($\sim$−1.65 to −1.31 eV) but more positive adsorption energies. The least favorable site is O[3Li2La], still with a sizeable $\Delta E_{ads}$ of $\sim$−1.31 eV.

Regardless of the binding oxygen site, the adsorbed $CO_2$ species reorganize into carbonate $CO_3^{2-}$ species after structural optimization. In detail, two oxygen atoms in $CO_2$ form bonds with metal ions available in the vicinity, with the carbonate species organizing in a polydentate conformation (Fig. S1†).[75] For all carbonates formed on the five sites, there are 13 bonds formed between surface metal ions and O of $CO_2$, including eight Li–O bonds and five La–O bonds. The higher number of Li–O bonds shows a clear preference for $Li^+$ over $La^{3+}$ ions. In particular, the surface carbonates show an average C–O bond length of $\sim$1.31 Å, comparable to $\sim$1.28 Å in bulk $Li_2CO_3$.[76]

The adsorption of $CO_2$ consists of two types of bonds: one between the carbon atom of $CO_2$ and a surface oxygen site, and the other between the oxygen atoms of $CO_2$ and metal ions of the surface. We observe that the incipient bond between O and metal ions on $Li_7La_3Zr_2O_{12}$ has major contributions to the values of $\Delta E_{ads}$. On different adsorption sites, the strength for the O and metal ion bonding depends on which metal ions are proximal to the site.

We also determined the bonding nature for $CO_2$ chemisorbed on $Li_7La_3Zr_2O_{12}$. Indeed, the dispersion contributions are calculated to be only $\sim$15–20%, similar to the cases of $H_2O$ adsorption discussed earlier. Charge transfer is then analyzed through the changes of Mulliken charges upon adsorption. Fig. S3† shows that the average changes are $\sim$0.30 for the surface O sites and $\sim$−0.26 for C in $CO_2$. Besides, the average change upon adsorption is $\sim$−0.22 for O in $CO_2$, $\sim$−0.01 for surface Li ions bonded to O, and $\sim$0.12 for La ions. These changes are slightly larger than those for $H_2O$ adsorption ($\sim$−0.05 for Li sites, $\sim$0.07 for La sites, and $\sim$0.03 for O in $H_2O$, see Fig. S3 in the ESI†). Taken together, this analysis confirms that the structural heterogeneity of surface sites on $Li_7La_3Zr_2O_{12}$ (010) enables strong adsorption of $H_2O$ and $CO_2$, which are otherwise known to physisorb on metals and ionic oxides. While such robust adsorption events are detrimental for the application of $Li_7La_3Zr_2O_{12}$ in energy storage, they indicate that $Li_7La_3Zr_2O_{12}$ is a potentially interesting catalyst support for $H_2O$ activation and adsorbing $CO_2$ from dilute streams.

We then studied $CO_2$ adsorption as a function of $CO_2$ coverage. $CO_2$ was sequentially adsorbed on all five O sites available on the $Li_7La_3Zr_2O_{12}$ surface. The sequential adsorption follows the order of their individual adsorption energies, from more negative to more positive (O[LiLaZr] (−2.21 eV) $\ll$ O[Li2La] (−1.65 eV) < O[LiLaZr] (−1.58 eV) < O[LiLaZr] (−1.34 eV) < O[3Li2La] (−1.31 eV)). In the process to adsorb the last $CO_2$ onto the $Li_7La_3Zr_2O_{12}$ surface, the O[3Li2La] site was found unfavorable, as adsorbed $CO_2$ on this site was too close ($\sim$1.20 Å) to $La^{3+}$ on the reconstructed surface. Eventually, there are only four out of five oxygen sites available for $CO_2$ adsorption, which set the highest $CO_2$ coverage to 4/5 ML. Besides the original five sites, less exposed O surface sites could increase the $CO_2$ coverage beyond 4/5 ML.

Table 2 shows the computed $\Delta E_{ads}$ for increasing the $CO_2$ loading up to the condition of 4/5 ML.

Fig. 4(a) shows the structure schematics and $\Delta\Omega$ diagram for each adsorption step toward the 4/5 ML coverage. $\Delta\Omega$ is defined as in eqn (3) and (4), and here it is calculated at 300 K and a $CO_2$ partial pressure of 1 bar.

In regimes of high-coverage, multiple $CO_2$ molecules interact with the surface in the same way as singly adsorbed $CO_2$ molecules, transforming into $CO_3^{2-}$ units. At the highest calculated coverage of 4/5 ML, all adsorbed $CO_2$ molecules react with the surface and form carbonates. As the coverage increases, $\Delta\Omega$ continuously decreases, indicating that the reaction between the surface and an increasing amount of $CO_2$ (up to 4/5 ML) is thermodynamically favorable. However, from Fig. 4, one observes that the absolute difference of $\Delta\Omega$ between consecutive steps decreases progressively, similar to the trends of Fig. 3(a). Fig. 4 and Table 2 show that each oxygen species at the $Li_7La_3Zr_2O_{12}$ surface becomes increasingly less reactive as the $CO_2$ coverage increases, which contributes to a progressive decrease of $\Delta E_{ads}$ and $\Delta\Omega$.

**Table 2** $CO_2$ adsorption energy (in eV per molecule) with increasing coverage of molecules (ML). The site is the adsorption site. $\delta\Delta E_{ads}$ indicates the change of $\Delta E_{ads}$ upon the addition of a $CO_2$ molecule. $CO_3^{2-}$ indicates whether the addition of a new $CO_2$ molecule promotes carbonate formation

| ML | Site | $\Delta E_{ads}$ | $\delta\Delta E_{ads}$ | $CO_3^{2-}$ |
|----|------|------------------|------------------------|-------------|
| 1/5 | O[LiLaZr] | −2.21 | — | Yes |
| 2/5 | O[Li2La] | −1.85 | +0.36 | Yes |
| 3/5 | O[LiLaZr] | −1.75 | +0.10 | Yes |
| 4/5 | O[LiLaZr] | −1.62 | +0.13 | Yes |

Fig. 4(b–d) show $\Delta\Omega$ at technologically relevant temperature and $CO_2$ partial pressures. As the temperature increases, the adsorption and reaction of $CO_2$ become less favorable, and the preferred coverage decreases from 4/5 ML to the conditions of $CO_2$-free surfaces. Similarly to the $H_2O$ case, at low temperature even higher $CO_2$ coverage than 4/5 ML may become accessible. However, this does not change significantly the situation of low $CO_2$-free surfaces at high temperature, as shown in Fig. 4(b–d). As the $CO_2$ partial pressure decreases from atmospheric to ultra-high vacuum, the formation of carbonates species at the $Li_7La_3Zr_2O_{12}$ surface appears less favorable, with the stability ranges of temperature expanding accordingly. This indicates that low $CO_2$ partial pressures are beneficial to minimize the carbonate contamination of the $Li_7La_3Zr_2O_{12}$ surface.

### 3.4. $CO_2$ and $H_2O$ co-adsorption on $Li_7La_3Zr_2O_{12}$

Having previously demonstrated the pronounced reactivity of the $Li_7La_3Zr_2O_{12}$ surface with $H_2O$ and $CO_2$, we verify the
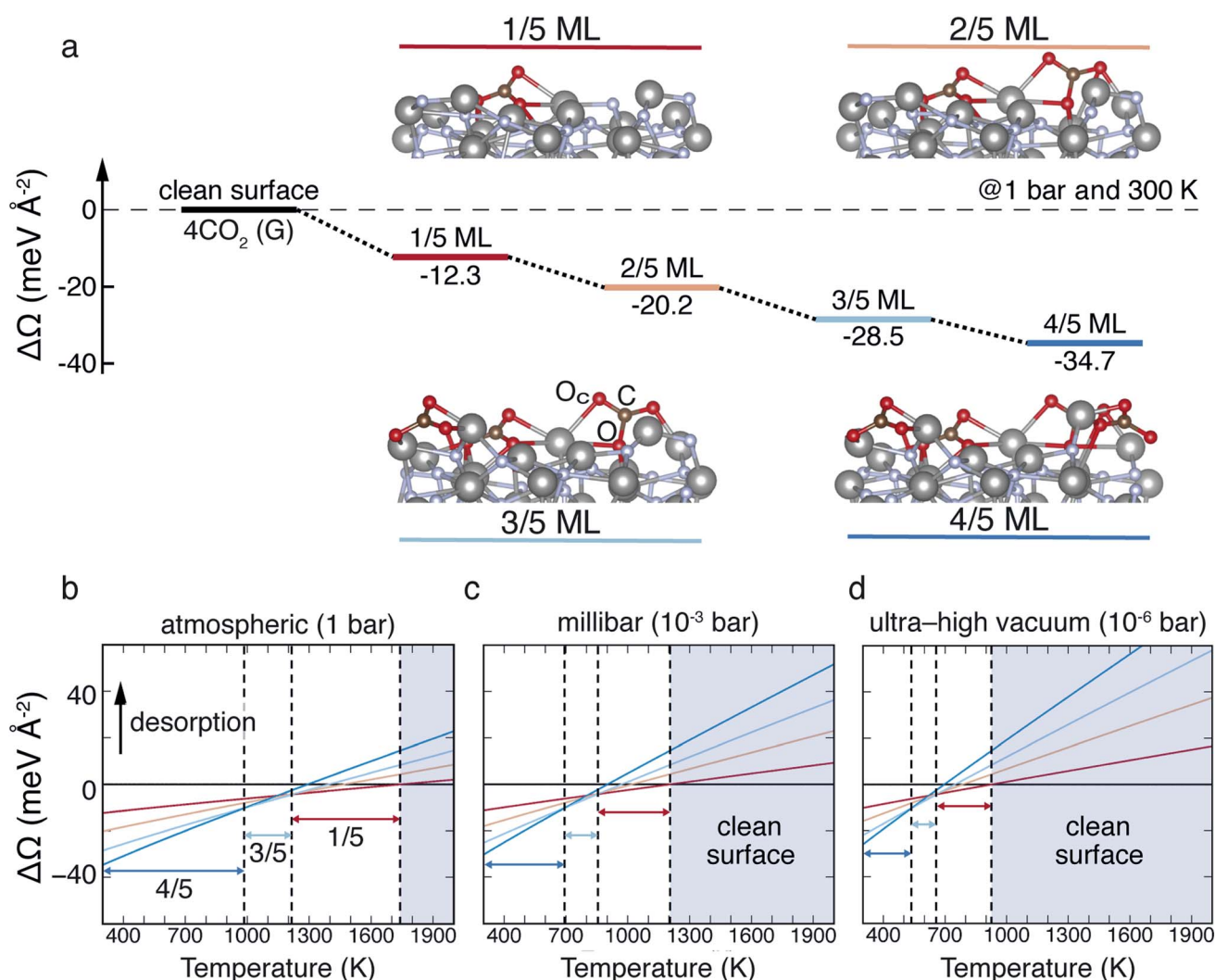


**Fig. 4** Change of grand potential $\Delta\Omega$ relative to a clean surface and gas-phase $CO_2$ at variable temperatures and pressures of technological relevance. In panel (a), the $CO_2$ coverage is denoted by a fraction of the $CO_2$ monolayer (ML) of the surface. $\Delta\Omega$ (in meV Å$^{-2}$) as a function of temperature for different $CO_2$ coverage and partial pressures of 1 (b, atmospheric regime), $1 \times 10^{-3}$ (c, millibar regime), and $1 \times 10^{-6}$ bar (d, ultra-high vacuum regime), respectively. Double arrows denote the most favorable coverage within each temperature range. The structures and $\Delta\Omega$ for different coverage are marked using the same color scheme of four divergent colors. Atomic species not directly involved in the adsorption are greyed out.

possibility of $H_2O$ and $CO_2$ reacting concurrently with the off-stoichiometric Li-terminated (010) cut.

We investigate the co-adsorption of $H_2O$ and $CO_2$ to mimic the hydroxide-mediated carbonation proposed in ref. 19, but here mediated explicitly by the $Li_7La_3Zr_2O_{12}$ surface. We adsorbed one $H_2O$ molecule on the most favorable site Li[3O] and then found the most favorable site to adsorb one $CO_2$ molecule on the same slab, see the inset in Fig. 5(a). In the co-adsorption model, the most favorable $CO_2$ site is O[LiLaZr] as for the case of individual $CO_2$ adsorption (see Section 3.3).

Next, we take the individual adsorption cases of $H_2O$ and $CO_2$ to represent the independent adsorption reactions (Fig. 5(b)). This situation corresponds to the infinitely separated adsorption of $H_2O$ and $CO_2$ molecules, with the two molecules not interacting with each other. Fig. 5(a) shows the $\Delta E_{ads}$ of the co-adsorption of $H_2O$ and $CO_2$, while Fig. 5(b) shows the $\Delta E_{ads}$s for infinitely separated $H_2O$ and $CO_2$ molecules.

The composed $\Delta E_{ads}$ of the individual adsorption energies of $H_2O$ ($\Delta E_{ads} \sim -1.21$ eV) and $CO_2$ ($\sim -2.21$ eV) is $\sim -3.42$ eV, which is more negative than the energy of co-adsorption, *i.e.*, $\sim -3.25$ eV. In the co-adsorption model of Fig. 5(a), the adsorbed $H_2O$ does not easily deprotonate, as opposed to the incipient $H_2O$ dissociation (at the same site) when adsorbed individually as in Fig. 5(b). This evidence clearly indicates that individual reactions of $H_2O$ and $CO_2$ with $Li_7La_3Zr_2O_{12}$ compete favorably against the concurrent co-adsorption of $H_2O$ and $CO_2$.
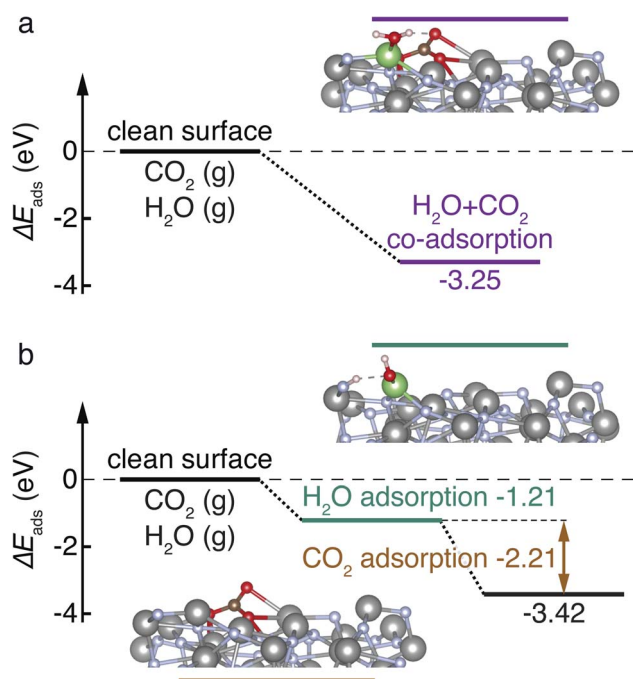


**Fig. 5** $\Delta E_{ads}$ for the adsorption of $H_2O$ and $CO_2$: (a) co-adsorption and (b) infinitely separated adsorption. The co-adsorption shows $\Delta E_{ads} = -3.25$ eV (in purple). The infinitely separated $H_2O$ adsorption ($\Delta E_{ads} = -1.21$ eV, in green) and $CO_2$ adsorption ($\Delta E_{ads} = -2.21$ eV, in brown) shows a combined adsorption energy of $\Delta E_{ads} = -3.42$ eV, more negative than the co-adsorption. The insets show schematic diagrams for adsorption structures. Atomic species not directly involved in the adsorption are greyed out.
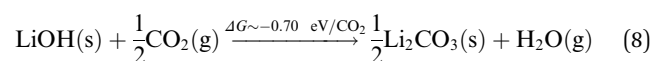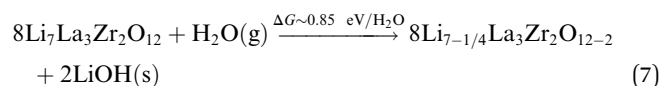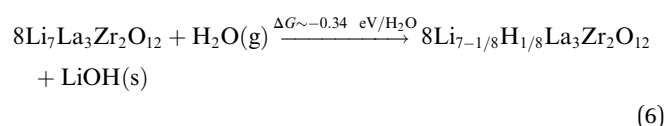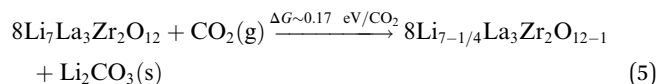
Therefore, the surface contamination of $Li_7La_3Zr_2O_{12}$ will be mostly driven by the independent reactions of direct hydration and direct carbonation, as opposed to the hydroxide-mediated carbonation proposed in ref. 19.

## 4.  Discussion

Using slab calculations in the framework of *ab initio* thermodynamics, we have explored the reactivity of the complex oxide $Li_7La_3Zr_2O_{12}$ with two ubiquitous molecules: $H_2O$ and $CO_2$. It is noted that all the adsorption processes investigated are barrier-free, which indicates the high reaction rates of $H_2O$ and $CO_2$ with $Li_7La_3Zr_2O_{12}$. A quantitative evaluation of the reaction rates requiring microkinetic models is beyond the scope of this study.

The exposure of $Li_7La_3Zr_2O_{12}$ to both $H_2O$ and $CO_2$ has been documented by preliminary computational and experimental studies.[14,19,21,77]

Using X-ray photo-emission spectroscopy (XPS) depth-profiling, Sharafi *et al.* showed the formation of $Li_2CO_3$ layers as thick as $\sim 5$–$10$ nm on the exterior of $Li_7La_3Zr_2O_{12}$ particles.[19] The authors proposed several chemical reactions (eqn 5–8) between $Li_7La_3Zr_2O_{12}$, $CO_2$ and $H_2O$, whose energetics ($\Delta G$s) were verified by first-principles calculations.[19] Nevertheless, the proposed reaction mechanisms of $Li_7La_3Zr_2O_{12}$ carbonation are still elusive requiring in-depth investigations, which justifies this endeavour.

$$8Li_7La_3Zr_2O_{12} + CO_2(g) \xrightarrow{\Delta G \sim 0.17 \ eV/CO_2} 8Li_{7-1/4}La_3Zr_2O_{12-1}$$
$$+ Li_2CO_3(s) \tag{5}$$

$$8Li_7La_3Zr_2O_{12} + H_2O(g) \xrightarrow{\Delta G \sim -0.34 \ eV/H_2O} 8Li_{7-1/8}H_{1/8}La_3Zr_2O_{12}$$
$$+ LiOH(s)$$
$$\tag{6}$$

$$8Li_7La_3Zr_2O_{12} + H_2O(g) \xrightarrow{\Delta G \sim 0.85 \ eV/H_2O} 8Li_{7-1/4}La_3Zr_2O_{12-2}$$
$$+ 2LiOH(s) \tag{7}$$

$$LiOH(s) + \frac{1}{2}CO_2(g) \xrightarrow{\Delta G \sim -0.70 \ eV/CO_2} \frac{1}{2}Li_2CO_3(s) + H_2O(g) \tag{8}$$

The $\Delta G$s in eqn (5)–(8) are from ref. 19. In eqn (5), $Li_2CO_3$ is directly formed *via* carbonation of $Li_7La_3Zr_2O_{12}$, but with a predicted positive $\Delta G$.[19] Compared to the unfavorable direct carbonation of $Li_7La_3Zr_2O_{12}$ (eqn (5)),[19] the hydroxide-mediated carbonation was interpreted as two favorable reactions: (i) the protonation of $Li_7La_3Zr_2O_{12}$ (eqn (6)) with $H^+$ exchanging with $Li^+$, followed by (ii) the conversion of LiOH and $CO_2$ into $Li_2CO_3$ as in eqn (8). Although with unfavorable $\Delta G$ ($\sim 0.85$ eV/$H_2O$), another mechanism proposed was the direct hydration of $Li_7La_3Zr_2O_{12}$ of eqn (7), which is followed by carbonation (of eqn (8)). Therefore, carbonate contamination on $Li_7La_3Zr_2O_{12}$ was proposed to form *via* the hydroxide-mediated pathway (eqn (6) and (8)) rather than direct carbonation (eqn (5)).[19]

In Section 3.2 and Table 1, we have amply demonstrated the favorable adsorption of $H_2O$ on the $Li_7La_3Zr_2O_{12}$ surface, with

spontaneous $H_2O$ dissociation on exposed $Li_{Surface}$ sites as $Li_{Surface}$–O–H, thus forming LiOH species. Our calculations clearly suggest that the formation of LiOH in $Li_7La_3Zr_2O_{12}$ is mediated by its reactive surface, which "catalyzes" the nucleation process of lithium hydroxide moieties. Indeed, XPS of $Li_7La_3Zr_2O_{12}$ particles has detected the signatures of $OH^-$ groups and LiOH even at relatively high temperatures (400–500 °C).[21]

Another pathway for LiOH formation proceeds through the protonation of Li–O moieties exposed at the $Li_7La_3Zr_2O_{12}$ surface, which we also predicted as a spontaneous process. The protonation of other M–O (with M = La or Zr) moieties at the $Li_7La_3Zr_2O_{12}$ surface may also form other adventitious species, whose signatures have not been reported yet. However, the available free protons at the surface (resulting from readily dissociated $H_2O$ molecules) can then be exchanged with $Li^+$ in $Li_7La_3Zr_2O_{12}$ as previously reported by thermo-gravimetric analysis mass-spectroscopy, neutron investigations, and focused ion beam secondary ion mass spectrometry.[14,77,78] Alternatively, proton species formed on the $Li_7La_3Zr_2O_{12}$ surface may intercalate directly into vacant $Li^+$ sites of the bulk structure. Note that the high Li-ion transport in $Li_7La_3Zr_2O_{12}$ facilitates $Li^+/H^+$ exchange.

$CO_3^{2-}$ contamination of the $Li_7La_3Zr_2O_{12}$ particle exteriors has been previously documented through Raman and XPS measurements.[19,21] Our calculations demonstrated spontaneous $CO_2$ adsorption and carbonate formation with the exposed oxygen atoms, i.e., $O_{Surface}$–$Li_{Surface}$ or $O_{Surface}$–$La_{Surface}$ (see Section 3.3 and Table 2) at the $Li_7La_3Zr_2O_{12}$ surface. This is in striking contrast to the unfavorable reaction of direct carbonation proposed in eqn (5).[21] Importantly, we show that the formation of $Li_2CO_3$ does not require the availability of LiOH for $CO_2$, but it is directly catalyzed by the $Li_7La_3Zr_2O_{12}$ surface. Our surface calculations show that carbonates are not limited to $Li_2CO_3$ species, instead incipient $CO_3^{2-}$ species may be bonded to other metal ions exposed at the surface of $Li_7La_3Zr_2O_{12}$, including Li and La. Therefore, the direct carbonation of $Li_7La_3Zr_2O_{12}$ is thermodynamically favorable and barrier-free. Notably, the co-adsorption of $H_2O$ and $CO_2$ appears less favorable than their individual adsorptions.

We have demonstrated the thermodynamically favorable processes of $H_2O$ and $CO_2$ decomposition on the $Li_7La_3Zr_2O_{12}$ particles. We use this knowledge to prescribe external conditions (temperature and pressure), which curb the LiOH and $Li_2CO_3$ contamination of $Li_7La_3Zr_2O_{12}$ during its synthesis. Fig. 6 shows the computed surface phase diagrams of $Li_7La_3Zr_2O_{12}$ as functions of temperature and partial pressures of $H_2O$ and $CO_2$. The derivation of the surface phase diagrams requires the minimization of the grand-potential energy of eqn (2) as the surface coverage, temperature, and pressure are varied.[24]

From Fig. 6, one clearly sees that the scenarios of high-$H_2O$ or $CO_2$ coverages are achieved at relatively high partial pressures ($\sim$2–10 bar) and low temperatures (<1000 K). Our predictions suggest that at atmospheric pressure ($\sim$1 bar) and at temperature above $\sim$1260 K, $Li_7La_3Zr_2O_{12}$ particles will be free of water, protons and LiOH species. The carbonation of $Li_7La_3Zr_2O_{12}$ appears more pernicious, which clearly requires higher temperatures above $\sim$1730 K for its complete elimination at atmospheric pressure (see Fig. 6(b)). These findings are representative of the real $Li_7La_3Zr_2O_{12}$ powder or the surface of sheets ($Li_7La_3Zr_2O_{12}$ composites), as the surface investigated dominates the $Li_7La_3Zr_2O_{12}$ Wulff shapes.[24,79]

The synthesis of $Li_7La_3Zr_2O_{12}$ is commonly carried out via the solid-state method, by calcination in "dry" air at temperatures $\sim$1000 °C ($\sim$1273 K).[19,21,23] The procedures of densification of $Li_7La_3Zr_2O_{12}$ via a hot press (or spark plasma) are regularly utilized to improve the contact between particles and increase the electrolyte ionic conductivity. The surface phase diagrams in Fig. 6 clearly show that both synthesis and sintering of $Li_7La_3Zr_2O_{12}$ should avoid air exposure. Notably, Fig. 6 shows that post-synthesis heat treatments (above 1000 °C) are beneficial to desorb $H_2O$ and eliminate other contaminants. Indeed, typical sintering temperatures for $Li_7La_3Zr_2O_{12}$ are in the range of 1000–1300 °C ($\sim$1300–1600 K).[19,23] Higher temperatures than 1300 °C may lead to significant Li (and proton) loss.[23] However, such elevated temperatures may still prevent the full removal of $Li_2CO_3$ at the surface. Li loss during the $Li_7La_3Zr_2O_{12}$ preparation is typically mitigated by adding LiOH and $Li_2CO_3$. Furthermore, we speculate that the addition of LiOH and $Li_2CO_3$ will not be disruptive to the preparation of $Li_7La_3Zr_2O_{12}$, and these two compounds may also limit their formation when $Li_7La_3Zr_2O_{12}$ is exposed to humid air.
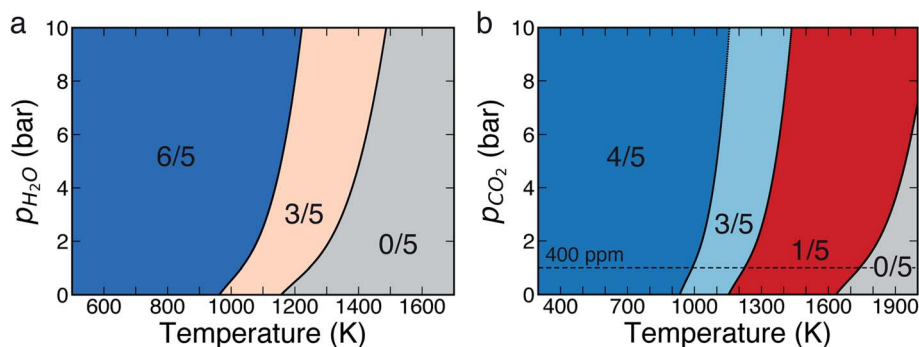


Fig. 6  Surface phase diagrams of $Li_7La_3Zr_2O_{12}$ at different temperatures and partial pressures of (a) $H_2O$ and (b) $CO_2$, respectively. Fractions of the monolayer (ML) and solid color denote the most favorable coverage scenarios within each range of temperature (in K) and partial pressure (in bar). The dashed line marks the $CO_2$ level of 400 ppm at a partial pressure of 1 bar. This line is used to indicate the thermodynamic favorability of adsorbing $CO_2$ from dilute streams, which is of relevance in $CO_2$ utilization.

Although the effect of partial pressure of $H_2O$ and $CO_2$ appears less significant than that of temperature with respect to $Li_7La_3Zr_2O_{12}$ contamination, synthesis under ultrahigh vacuum conditions ($\sim 1 \times 10^{-6}$ bar) and at $\sim 800$ K guarantees a water-free $Li_7La_3Zr_2O_{12}$ surface, which is sparsely contaminated by $Li_2CO_3$ species. Clearly, these conditions appear unpractical, but glove-box synthesis at pressures within mbar ranges (see Fig. 3 and 4) may be more accessible and deserve further investigations.

Fig. 6 indicates external conditions, which favor (010) $Li_7La_3Zr_2O_{12}$ surfaces decorated with dissociated $H_2O$ and carbonate species. While these surfaces may not be desired for energy storage applications, the strong adsorption of $CO_2$ and $H_2O$ suggests that the off-stoichiometric (010) surface of $Li_7La_3Zr_2O_{12}$ can serve as a support in catalysis. Using two examples of the water gas shift reaction and $CO_2$ utilisation, we elaborate further below. The water-gas shift reaction is typically catalyzed by noble metal nanoparticles stabilized by oxide supports. Experimental and theoretical studies have indicated that the oxide supports facilitate $H_2O$ dissociation,[44,45] a critical elementary step in this reaction. The favorable adsorption of $H_2O$ and its spontaneous dissociation thus make $Li_7La_3Zr_2O_{12}$ a promising support for the water-gas shift reaction. Indeed, there is a concerted effort to design catalytic systems, which operate under dilute streams of $CO_2$.[46,47] Fig. 6 illustrates that at 500–600 K, 4/5 ML of $CO_2$ is adsorbed on $Li_7La_3Zr_2O_{12}$ even at $CO_2$ pressures as low as 400 ppm. Hence, the strong adsorption strength of $CO_2$ on $Li_7La_3Zr_2O_{12}$ makes this material a promising support for dual-functional catalysts, which adsorb $CO_2$ from dilute streams and further hydrogenate it to chemicals, such as methanol and ethylene over metal nanoparticles dispersed on $Li_7La_3Zr_2O_{12}$.

## 5. Conclusions

In summary, using a robust *ab initio* thermodynamic framework, we investigated the complex surface reactivity of $Li_7La_3Zr_2O_{12}$ toward ubiquitous $H_2O$ and $CO_2$. The Li-terminated off-stoichiometric surface of $Li_7La_3Zr_2O_{12}$ readily reacts with $H_2O$ and $CO_2$, which promotes the direct formation of metal hydroxide and carbonate species. We demonstrated that synthesis within a mbar pressure range can lead to a water-free $Li_7La_3Zr_2O_{12}$ surface and reduce drastically the amount of carbonates formed. Our in-depth analysis provides strategies and opportunities to improve the synthesis conditions of $Li_7La_3Zr_2O_{12}$ and similar complex oxides with high technological relevance to batteries and catalysis. The strong adsorption of $CO_2$ under conditions of low partial pressure and $H_2O$ indicates the potential of $Li_7La_3Zr_2O_{12}$ as a suitable catalyst support for the hydrogenation of dilute $CO_2$ streams and the water-gas shift reaction respectively. These findings are general and provide rules of thumb to analyze the reactivity of complex oxides toward two common molecules, *i.e.*, $H_2O$ and $CO_2$.

## Conflicts of interest

There are no conflicts to declare.

## References

1 B. Dunn, H. Kamath and J.-M. Tarascon, Electrical Energy Storage for the Grid: A Battery of Choices, *Science*, 2011, **334**, 928–935.

2 B. Nykvist and M. Nilsson, Rapidly Falling Costs of Battery Packs for Electric Vehicles, *Nat. Clim. Change*, 2015, **5**, 329–332.

3 Z. P. Cano, D. Banham, S. Ye, A. Hintennach, J. Lu, M. Fowler and Z. Chen, Batteries and Fuel Cells for Emerging Electric Vehicle Markets, *Nat. Energy*, 2018, **3**, 279–289.

4 R. E. Warburton, J. J. Kim, S. Patel, J. D. Howard, L. A. Curtiss, C. Wolverton, D. B. Buchholz, J. T. Vaughey, P. Fenter, T. T. Fister and J. Greeley, Tailoring Interfaces in Solid-State Batteries Using Interfacial Thermochemistry and Band Alignment, *Chem. Mater.*, 2021, **33**, 8447–8459.

5 J. B. Goodenough and Y. Kim, Challenges for Rechargeable Li Batteries, *Chem. Mater.*, 2010, **22**, 587–603.

6 J. C. Bachman, S. Muy, A. Grimaud, H.-H. Chang, N. Pour, S. F. Lux, O. Paschos, F. Maglia, S. Lupart, P. Lamp, L. Giordano and Y. Shao-Horn, Inorganic Solid-State Electrolytes for Lithium Batteries: Mechanisms and Properties Governing Ion Conduction, *Chem. Rev.*, 2016, **116**, 140–162.

7 Z. Zhang, Y. Shao, B. Lotsch, Y.-S. Hu, H. Li, J. Janek, L. F. Nazar, C.-W. Nan, J. Maier, M. Armand and L. Chen, New Horizons for Inorganic Solid State Ion Conductors, *Energy Environ. Sci.*, 2018, **11**, 1945–1976.

8 J. Janek and W. G. Zeier, A Solid Future for Battery Development, *Nat. Energy*, 2016, **1**, 16141.

9 T. Famprikis, P. Canepa, J. A. Dawson, M. S. Islam and C. Masquelier, Fundamentals of Inorganic Solid-State Electrolytes for Batteries, *Nat. Mater.*, 2019, **18**, 1278–1291.

10 V. Thangadurai, H. Kaack and W. J. F. Weppner, Novel Fast Lithium Ion Conduction in Garnet-Type $Li_5La_3M_2O_{12}$ (M = Nb, Ta), *J. Am. Ceram. Soc.*, 2003, **86**, 437–440.

11 R. Murugan, V. Thangadurai and W. Weppner, Fast Lithium Ion Conduction in Garnet-Type $Li_7La_3Zr_2O_{12}$, *Angew. Chem., Int. Ed.*, 2007, **46**, 7778–7781.

12 H. Buschmann, J. Dölle, S. Berendts, A. Kuhn, P. Bottke, M. Wilkening, P. Heitjans, A. Senyshyn, H. Ehrenberg, A. Lotnyk, V. Duppel, L. Kienle and J. Janek, Structure and Dynamics of the Fast Lithium Ion Conductor "$Li_7La_3Zr_2O_{12}$", *Phys. Chem. Chem. Phys.*, 2011, **13**, 19378.

13 S. Toda, K. Ishiguro, Y. Shimonishi, A. Hirano, Y. Takeda, O. Yamamoto and N. Imanishi, Low Temperature Cubic Garnet-Type CO2-Doped $Li_7La_3Zr_2O_{12}$, *Solid State Ionics*, 2013, **233**, 102–106.

14 C. Galven, J. Dittmer, E. Suard, F. Le Berre and M.-P. Crosnier-Lopez, Instability of Lithium Garnets against Moisture. Structural Characterization and Dynamics of $Li_{7-x}H_xLa_3Sn_2O_{12}$ and $Li_{5-x}H_xLa_3Nb_2O_{12}$, *Chem. Mater.*, 2012, **24**, 3335–3345.

15 J. Allen, J. Wolfenstine, E. Rangasamy and J. Sakamoto, Effect of Substitution (Ta, Al, Ga) on the Conductivity of $Li_7La_3Zr_2O_{12}$, *J. Power Sources*, 2012, **206**, 315–319.

16 V. Thangadurai, S. Narayanan and D. Pinzaru, Garnet-Type Solid-State Fast Li Ion Conductors for Li Batteries: Critical Review, *Chem. Soc. Rev.*, 2014, **43**, 4714.

17 S. Mukhopadhyay, T. Thompson, J. Sakamoto, A. Huq, J. Wolfenstine, J. L. Allen, N. Bernstein, D. A. Stewart and M. D. Johannes, Structure and Stoichiometry in Supervalent Doped $Li_7La_3Zr_2O_{12}$, *Chem. Mater.*, 2015, **27**, 3658–3665.

18 L. Cheng, C. H. Wu, A. Jarry, W. Chen, Y. Ye, J. Zhu, R. Kostecki, K. Persson, J. Guo, M. Salmeron, G. Chen and M. Doeff, Interrelationships among Grain Size, Surface Composition, Air Stability, and Interfacial Resistance of Al-Substituted $Li_7La_3Zr_2O_{12}$ Solid Electrolytes, *ACS Appl. Mater. Interfaces*, 2015, **7**, 17649–17655.

19 A. Sharafi, S. Yu, M. Naguib, M. Lee, C. Ma, H. M. Meyer, J. Nanda, M. Chi, D. J. Siegel and J. Sakamoto, Impact of Air Exposure and Surface Chemistry on $Li–Li_7La_3Zr_2O_{12}$ Interfacial Resistance, *J. Mater. Chem. A*, 2017, **5**, 13475–13487.

20 L. Porz, T. Swamy, B. W. Sheldon, D. Rettenwander, T. Frömling, H. L. Thaman, S. Berendts, R. Uecker, W. C. Carter and Y.-M. Chiang, Mechanism of Lithium Metal Penetration through Inorganic Solid Electrolytes, *Adv. Energy Mater.*, 2017, **7**, 1701003.

21 A. Sharafi, E. Kazyak, A. L. Davis, S. Yu, T. Thompson, D. J. Siegel, N. P. Dasgupta and J. Sakamoto, Surface Chemistry Mechanism of Ultra-Low Interfacial Resistance in the Solid-State Electrolyte $Li_7La_3Zr_2O_{12}$, *Chem. Mater.*, 2017, **29**, 7961–7968.

22 X. Han, Y. Gong, K. K. Fu, X. He, G. T. Hitz, J. Dai, A. Pearse, B. Liu, H. Wang, G. Rubloff, Y. Mo, V. Thangadurai, E. D. Wachsman and L. Hu, Negating Interfacial Impedance in Garnet-Based Solid-State Li Metal Batteries, *Nat. Mater.*, 2017, **16**, 572–579.

23 A. Sharafi, C. G. Haslam, R. D. Kerns, J. Wolfenstine and J. Sakamoto, Controlling and Correlating the Effect of Grain Size with the Mechanical and Electrochemical Properties of $Li_7La_3Zr_2O_{12}$ Solid-State Electrolyte, *J. Mater. Chem. A*, 2017, **5**, 21491–21504.

24 P. Canepa, J. A. Dawson, G. Sai Gautam, J. M. Statham, S. C. Parker and M. S. Islam, Particle Morphology and Lithium Segregation to Surfaces of the $Li_7La_3Zr_2O_{12}$ Solid Electrolyte, *Chem. Mater.*, 2018, **30**, 3019–3027.

25 J. Kasemchainan, S. Zekoll, D. Spencer Jolly, Z. Ning, G. O. Hartley, J. Marrow and P. G. Bruce, Critical Stripping Current Leads to Dendrite Formation on Plating in Lithium Anode Solid Electrolyte Cells, *Nat. Mater.*, 2019, **18**, 1105–1111.

26 L. Annamalai, Y. Liu, S. Ezenwa, Y. Dang, S. L. Suib and P. Deshlahra, Influence of Tight Confinement on Selective Oxidative Dehydrogenation of Ethane on MoVTeNb Mixed Oxides, *ACS Catal.*, 2018, **8**, 7051–7067.

27 R. B. Licht and A. T. Bell, A DFT Investigation of the Mechanism of Propene Ammoxidation over $\alpha$-Bismuth Molybdate, *ACS Catal.*, 2017, **7**, 161–176.

28 C. Brookes, P. P. Wells, G. Cibin, N. Dimitratos, W. Jones, D. J. Morgan and M. Bowker, Molybdenum Oxide on $Fe_2O_3$ Core–Shell Catalysts: Probing the Nature of the Structural Motifs Responsible for Methanol Oxidation Catalysis, *ACS Catal.*, 2014, **4**, 243–250.

29 X. Li, D. Teschner, V. Streibel, T. Lunkenbein, L. Masliuk, T. Fu, Y. Wang, T. Jones, F. Seitz, F. Girgsdies, F. Rosowski, R. Schlögl and A. Trunschke, How to Control Selectivity in Alkane Oxidation?, *Chem. Sci.*, 2019, **10**, 2429–2443.

30 A. Trunschke, J. Noack, S. Trojanov, F. Girgsdies, T. Lunkenbein, V. Pfeifer, M. Hävecker, P. Kube, C. Sprung, F. Rosowski and R. Schlögl, The Impact of the Bulk Structure on Surface Dynamics of Complex Mo–V-Based Oxide Catalysts, *ACS Catal.*, 2017, **7**, 3061–3071.

31 Y. Li, Q. Fu and M. Flytzani-Stephanopoulos, Low-Temperature Water-Gas Shift Reaction over Cu- and Ni-Loaded Cerium Oxide Catalysts, *Appl. Catal., B*, 2000, **27**, 179–191.

32 Y. Tanaka, Water Gas Shift Reaction for the Reformed Fuels over Cu/MnO Catalysts Prepared *via* Spinel-Type Oxide, *J. Catal.*, 2003, **215**, 271–278.

33 J. Papavasiliou, G. Avgouropoulos and T. Ioannides, Combined Steam Reforming of Methanol over Cu–Mn Spinel Oxide Catalysts, *J. Catal.*, 2007, **251**, 7–20.

34 J. A. Rodriguez, S. Ma, P. Liu, J. Hrbek, J. Evans and M. Pérez, Activity of $CeO_x$ and $TiO_x$ Nanoparticles Grown on Au(111) in the Water-Gas Shift Reaction, *Science*, 2007, **318**, 1757–1760.

35 J. Rodriguez, P. Liu, X. Wang, W. Wen, J. Hanson, J. Hrbek, M. Pérez and J. Evans, Water-Gas Shift Activity of Cu Surfaces and Cu Nanoparticles Supported on Metal Oxides, *Catal. Today*, 2009, **143**, 45–50.

36 E. W. McFarland and H. Metiu, Catalysis by Doped Oxides, *Chem. Rev.*, 2013, **113**, 4391–4427.

37 N. C. Nelson, M.-T. Nguyen, V.-A. Glezakou, R. Rousseau and J. Szanyi, Carboxyl Intermediate Formation *via* an *in situ*-Generated Metastable Active Site during Water-Gas Shift Catalysis, *Nat. Catal.*, 2019, **2**, 916–924.

38 S. Wang, G. Q. M. Lu and G. J. Millar, Carbon Dioxide Reforming of Methane To Produce Synthesis Gas over Metal-Supported Catalysts: State of the Art, *Energy Fuels*, 1996, **10**, 896–904.

39 H. Muroyama, Y. Tsuda, T. Asakoshi, H. Masitah, T. Okanishi, T. Matsui and K. Eguchi, Carbon Dioxide Methanation over Ni Catalysts Supported on Various Metal Oxides, *J. Catal.*, 2016, **343**, 178–184.

40 E.-h. Yang, Y. S. Noh, G. H. Hong and D. J. Moon, Combined Steam and $CO_2$ Reforming of Methane over $La_{1-x}Sr_xNiO_3$ Perovskite Oxides, *Catal. Today*, 2018, **299**, 242–250.

41 A. R. Derk, G. M. Moore, S. Sharma, E. W. McFarland and H. Metiu, Catalytic Dry Reforming of Methane on Ruthenium-Doped Ceria and Ruthenium Supported on Ceria, *Top. Catal.*, 2014, **57**, 118–124.

42 J. Wang, G. Li, Z. Li, C. Tang, Z. Feng, H. An, H. Liu, T. Liu and C. Li, A Highly Selective and Stable $ZnO–ZrO_2$ Solid Solution Catalyst for $CO_2$ Hydrogenation to Methanol, *Sci. Adv.*, 2017, **3**, e1701290.

43 M. Huš, D. Kopač and B. Likozar, Catalytic Hydrogenation of Carbon Dioxide to Methanol: Synergistic Effect of Bifunctional Cu/Perovskite Catalysts, *ACS Catal.*, 2019, **9**, 105–116.

44 Z.-J. Zhao, Z. Li, Y. Cui, H. Zhu, W. F. Schneider, W. N. Delgass, F. Ribeiro and J. Greeley, Importance of Metal-Oxide Interfaces in Heterogeneous Catalysis: A Combined DFT, Microkinetic, and Experimental Study of Water-Gas Shift on Au/MgO, *J. Catal.*, 2017, **345**, 157–169.

45 N. C. Nelson and J. Szanyi, Heterolytic Hydrogen Activation: Understanding Support Effects in Water-Gas Shift, Hydrodeoxygenation, and CO Oxidation Catalysis, *ACS Catal.*, 2020, **10**, 5663–5671.

46 R. Sen, A. Goeppert, S. Kar and G. K. S. Prakash, Hydroxide Based Integrated $CO_2$ Capture from Air and Conversion to Methanol, *J. Am. Chem. Soc.*, 2020, **142**, 4544–4549.

47 I. S. Omodolor, H. O. Otor, J. A. Andonegui, B. J. Allen and A. C. Alba-Rubio, Dual-Function Materials for $CO_2$ Capture and Conversion: A Review, *Ind. Eng. Chem. Res.*, 2020, **59**, 17612–17631.

48 W. Kohn and L. J. Sham, Self-Consistent Equations Including Exchange and Correlation Effects, *Phys. Rev.*, 1965, **140**, A1133–A1138.

49 J. P. Perdew, K. Burke and M. Ernzerhof, Generalized Gradient Approximation Made Simple, *Phys. Rev. Lett.*, 1996, **77**, 3865–3868.

50 S. Grimme, J. Antony, S. Ehrlich and H. Krieg, A Consistent and Accurate *Ab Initio* Parametrization of Density Functional Dispersion Correction (DFT-D) for the 94 Elements H-Pu, *J. Chem. Phys.*, 2010, **132**, 154104.

51 S. Grimme, S. Ehrlich and L. Goerigk, Effect of the Damping Function in Dispersion Corrected Density Functional Theory, *J. Comput. Chem.*, 2011, **32**, 1456–1465.

52 A. D. Becke and E. R. Johnson, Exchange-Hole Dipole Moment and the Dispersion Interaction Revisited, *J. Chem. Phys.*, 2007, **127**, 154108.

53 G. Kresse and J. Furthmüller, Efficiency of *Ab Initio* Total Energy Calculations for Metals and Semiconductors Using a Plane-Wave Basis Set, *Comput. Mater. Sci.*, 1996, **6**, 15–50.

54 G. Kresse and J. Furthmüller, Efficient Iterative Schemes for *Ab Initio* Total-Energy Calculations Using a Plane-Wave Basis Set, *Phys. Rev. B: Condens. Matter Mater. Phys.*, 1996, **54**, 11169–11186.

55 G. Kresse and J. Hafner, *Ab Initio* Molecular Dynamics for Liquid Metals, *Phys. Rev. B: Condens. Matter Mater. Phys.*, 1993, **47**, 558–561.

56 G. Kresse and D. Joubert, From Ultrasoft Pseudopotentials to the Projector Augmented-Wave Method, *Phys. Rev. B: Condens. Matter Mater. Phys.*, 1999, **59**, 1758–1775.

57 T. S. Choksi, L. T. Roling, V. Streibel and F. Abild-Pedersen, Predicting Adsorption Properties of Catalytic Descriptors on Bimetallic Nanoalloys with Site-Specific Precision, *J. Phys. Chem. Lett.*, 2019, **10**, 1852–1859.

58 S. Maintz, V. L. Deringer, A. L. Tchougréeff and R. Dronskowski, LOBSTER: A Tool to Extract Chemical Bonding from Plane-Wave Based DFT: Tool to Extract Chemical Bonding, *J. Comput. Chem.*, 2016, **37**, 1030–1035.

59 K. T. Butler, G. Sai Gautam and P. Canepa, Designing Interfaces in Energy Materials Applications with First-Principles Calculations, *npj Comput. Mater.*, 2019, **5**, 19.

60 Chase, M. W., National Institute of Standards and Technology (U.S.), Issued as: Journal of physical and chemical reference data; monograph no. 9, *NIST-JANAF Thermochemical Tables*, American Chemical Society, American Institute of Physics for the National Institute of Standards and Technology, Washington, DC, New York, 4th edn, 1998.

61 S. P. Ong, W. D. Richards, A. Jain, G. Hautier, M. Kocher, S. Cholia, D. Gunter, V. L. Chevrier, K. A. Persson and G. Ceder, Python Materials Genomics (Pymatgen): A Robust, Open-Source Python Library for Materials Analysis, *Comput. Mater. Sci.*, 2013, **68**, 314–319.

62 P. W. Tasker, The Stability of Ionic Crystal Surfaces, *J. Phys. C: Solid State Phys.*, 1979, **12**, 4977–4984.

63 A. Szabo and N. S. Ostlund, *Modern Quantum Chemistry: Introduction to Advanced Electronic Structure Theory*, Dover Publications, Mineola, N. Y., 1996.

64 R. G. Parr and R. G. Pearson, Absolute Hardness: Companion Parameter to Absolute Electronegativity, *J. Am. Chem. Soc.*, 1983, **105**, 7512–7516.

65 R. Dronskowski, *Computational Chemistry of Solid State Materials: A Guide for Materials Scientists, Chemists, Physicists and Others*, 1st edn, Wiley, 2005.

66 Z.-T. Wang, Y.-G. Wang, R. Mu, Y. Yoon, A. Dahal, G. K. Schenter, V.-A. Glezakou, R. Rousseau, I. Lyubinetsky and Z. Dohnálek, Probing Equilibrium of Molecular and Deprotonated Water on $TiO_2$ (110), *Proc. Natl. Acad. Sci. U. S. A.*, 2017, **114**, 1801–1805.

67 M. F. Calegari Andrade, H.-Y. Ko, L. Zhang, R. Car and A. Selloni, Free Energy of Proton Transfer at the Water–$TiO_2$ Interface from *Ab Initio* Deep Potential Molecular Dynamics, *Chem. Sci.*, 2020, **11**, 2335–2341.

68 M.-T. Nguyen, R. Mu, D. C. Cantu, I. Lyubinetsky, V.-A. Glezakou, Z. Dohnálek and R. Rousseau, Dynamics, Stability, and Adsorption States of Water on Oxidized $RuO_2$ (110), *J. Phys. Chem. C*, 2017, **121**, 18505–18515.

69 T. Choksi and J. Greeley, Partial Oxidation of Methanol on $MoO_3$ (010): A DFT and Microkinetic Study, *ACS Catal.*, 2016, **6**, 7260–7277.

70 H. Metiu, S. Chrétien, Z. Hu, B. Li and X. Sun, Chemistry of Lewis Acid–Base Pairs on Oxide Surfaces, *J. Phys. Chem. C*, 2012, **116**, 10439–10450.

71 A. Kakekhani, L. T. Roling, A. Kulkarni, A. A. Latimer, H. Abroshan, J. Schumann, H. AlJama, S. Siahrostami, S. Ismail-Beigi, F. Abild-Pedersen and J. K. Nørskov, Nature of Lone-Pair–Surface Bonds and Their Scaling Relations, *Inorg. Chem.*, 2018, **57**, 7222–7238.

72 R. Mu, D. C. Cantu, X. Lin, V.-A. Glezakou, Z. Wang, I. Lyubinetsky, R. Rousseau and Z. Dohnálek, Dimerization Induced Deprotonation of Water on RuO$_2$ (110), *J. Phys. Chem. Lett.*, 2014, **5**, 3445–3450.

73 R. Mu, D. C. Cantu, V.-A. Glezakou, I. Lyubinetsky, R. Rousseau and Z. Dohnálek, Deprotonated Water Dimers: The Building Blocks of Segmented Water Chains on Rutile RuO$_2$ (110), *J. Phys. Chem. C*, 2015, **119**, 23552–23558.

74 I. M. Nadeem, J. P. W. Treacy, S. Selcuk, X. Torrelles, H. Hussain, A. Wilson, D. C. Grinter, G. Cabailh, O. Bikondoa, C. Nicklin, A. Selloni, J. Zegenhagen, R. Lindsay and G. Thornton, Water Dissociates at the Aqueous Interface with Reduced Anatase TiO$_2$ (101), *J. Phys. Chem. Lett.*, 2018, **9**, 3131–3136.

75 H. Tsuji, A. Okamura-Yoshida, T. Shishido and H. Hattori, Dynamic Behavior of Carbonate Species on Metal Oxide Surface: Oxygen Scrambling between Adsorbed Carbon Dioxide and Oxide Surface, *Langmuir*, 2003, **19**, 8793–8800.

76 Y. Idemoto, J. W. Richardson, N. Koura, S. Kohara and C.-K. Loong, Crystal Structure of $(Li_xK_{1-x})_2CO_3$ (x = 0, 0.43, 0.5, 0.62, 1) by Neutron Powder Diffraction Analysis, *J. Phys. Chem. Solids*, 1998, **59**, 363–376.

77 G. Larraz, A. Orera and M. L. Sanjuán, Cubic Phases of Garnet-Type Li$_7$La$_3$Zr$_2$O$_{12}$: The Role of Hydration, *J. Mater. Chem. A*, 2013, **1**, 11419.

78 R. H. Brugge, A. K. O. Hekselman, A. Cavallaro, F. M. Pesci, R. J. Chater, J. A. Kilner and A. Aguadero, Garnet Electrolytes for Solid State Batteries: Visualization of Moisture-Induced Chemical Degradation and Revealing Its Impact on the Li-Ion Dynamics, *Chem. Mater.*, 2018, **30**, 3704–3713.

79 J. Awaka, N. Kijima, H. Hayakawa and J. Akimoto, Synthesis and Structure Analysis of Tetragonal Li$_7$La$_3$Zr$_2$O$_{12}$ with the Garnet-Related Type Structure, *J. Solid State Chem.*, 2009, **182**, 2046–2052.